The Astrophysical Journal, 974:50 (16pp), 2024 October 10 https://doi.org/10.3847/1538-4357/ad63a1

X-Ray and Multiwavelength Polarization of Mrk 501 from 2022 to 2023

Chien-Ting J. Chen[1,2], Ioannis Liodakis[3,4], Riccardo Middei[5,6], Dawoon E. Kim[7,8,9], Laura Di Gesu[10], Alessandro Di Marco[7], Steven R. Ehlert[3], Manel Errando[11], Michela Negro[12], Svetlana G. Jorstad[13,14], Alan P. Marscher[13], Kinwah Wu[15], Iván Agudo[16], Juri Poutanen[17], Tsunefumi Mizuno[18], Pouya M. Kouch[17,19,20], Elina Lindfors[17], George A. Borman[21], Tatiana S. Grishina[14], Evgenia N. Kopatskaya[14], Elena G. Larionova[14], Daria A. Morozova[14], Sergey S. Savchenko[14,22], Ivan S. Troitsky[14], Yulia V. Troitskaya[14], Andrey A. Vasilyev[14], Alexey V. Zhovtan[21], Francisco José Aceituno[23], Giacomo Bonnoli[23,24], Víctor Casanova[23], Juan Escudero[23], Beatriz Agís-González[4,23], César Husillos[25], Jorge Otero Santos[23], Alfredo Sota[23], Vilppu Piirola[17], Ioannis Myserlis[26,27], Emmanouil Angelakis[28], Alexander Kraus[27], Mark Gurwell[29], Garrett Keating[29], Ramprasad Rao[29], Sincheol Kang[30], Sang-Sung Lee[30,31], Sang-Hyun Kim[30,31], Whee Yeon Cheong[30,31], Hyeon-Woo Jeong[30,31], Chanwoo Song[30,31], Andrei V. Berdyugin[17], Masato Kagitani[32], Vadim Kravtsov[17], Anagha P. Nitindala[17], Takeshi Sakanoi[32], Ryo Imazawa[33], Mahito Sasada[34], Yasushi Fukazawa[33,35,36], Koji S. Kawabata[33,35,36], Makoto Uemura[33,35,36], Tatsuya Nakaoka[35], Hiroshi Akitaya[37], Carolina Casadio[38,39], Albrecht Sievers[26], Lucio Angelo Antonelli[5,40], Matteo Bachetti[41], Luca Baldini[42,43], Wayne H. Baumgartner[3], Ronaldo Bellazzini[42], Stefano Bianchi[44], Stephen D. Bongiorno[3], Raffaella Bonino[45,46], Alessandro Brez[42], Niccoló Bucciantini[47,48,49], Fiamma Capitanio[7], Simone Castellano[42], Elisabetta Cavazzuti[10], Stefano Ciprini[5,50], Enrico Costa[7], Alessandra De Rosa[7], Ettore Del Monte[7], Niccoló Di Lalla[51], Immacolata Donnarumma[10], Victor Doroshenko[52], Michal Dovčiak[53], Teruaki Enoto[54], Yuri Evangelista[55], Sergio Fabiani[7], Riccardo Ferrazzoli[7], Javier A. Garcia[56], Shuichi Gunji[57], Kiyoshi Hayashida[58], Jeremy Heyl[59], Wataru Iwakiri[60], Philip Kaaret[3], Vladimir Karas[53], Fabian Kislat[61], Takao Kitaguchi[54], Jeffery J. Kolodziejczak[3], Henric Krawczynski[11], Fabio La Monaca[7,62,63], Luca Latronico[45], Simone Maldera[45], Alberto Manfreda[64], Frédéric Marin[65], Andrea Marinucci[10], Herman L. Marshall[66], Francesco Massaro[45,46], Giorgio Matt[44], Ikuyuki Mitsuishi[67], Fabio Muleri[7], C.-Y. Ng[68], Stephen L. O'Dell[3], Nicola Omodei[51], Chiara Oppedisano[45], Alessandro Papitto[40], George G. Pavlov[69], Abel Lawrence Peirson[51], Matteo Perri[5,40], Melissa Pesce-Rollins[42], Pierre-Olivier Petrucci[70], Maura Pilia[41], Andrea Possenti[41], Simonetta Puccetti[5], Brian D. Ramsey[3], John Rankin[7], Ajay Ratheesh[7], Oliver J. Roberts[1], Roger W. Romani[51], Carmelo Sgró[42], Patrick Slane[71], Paolo Soffitta[7], Gloria Spandre[42], Douglas A. Swartz[1], Toru Tamagawa[54], Fabrizio Tavecchio[24], Roberto Taverna[72], Yuzuru Tawara[67], Allyn F. Tennant[3], Nicholas E. Thomas[3], Francesco Tombesi[50,62], Alessio Trois[41], Sergey S. Tsygankov[17], Roberto Turolla[15,72], Jacco Vink[73], Martin C. Weisskopf[3], Fei Xie[7,74], and Silvia Zane[15]

[1] Science and Technology Institute, Universities Space Research Association, Huntsville, AL 35805, USA
[2] Astrophysics Office, NASA Marshall Space Flight Center, ST12, Huntsville, AL 35812, USA
[3] NASA Marshall Space Flight Center, Huntsville, AL 35812, USA
[4] Institute of Astrophysics, Foundation for Research and Technology-Hellas, GR-70013 Heraklion, Greece
[5] Space Science Data Center, Agenzia Spaziale Italiana, Via del Politecnico snc, 00133 Roma, Italy
[6] INAF Osservatorio Astronomico di Roma, Via Frascati 33, 00040 Monte Porzio Catone (RM), Italy
[7] INAF Istituto di Astrofisica e Planetologia Spaziali, Via del Fosso del Cavaliere 100, 00133 Roma, Italy
[8] Dipartimento di Fisica, Università degli Studi di Roma "La Sapienza", Piazzale Aldo Moro 5, 00185 Roma, Italy
[9] Dipartimento di Fisica, Università degli Studi di Roma "Tor Vergata", Via della Ricerca Scientifica 1, 00133 Roma, Italy
[10] ASI - Agenzia Spaziale Italiana, Via del Politecnico snc, 00133 Roma, Italy
[11] Physics Department and McDonnell Center for the Space Sciences, Washington University in St. Louis, St. Louis, MO 63130, USA
[12] Department of Physics and Astronomy, Louisiana State University, Baton Rouge, LA 70803, USA
[13] Institute for Astrophysical Research, Boston University, 725 Commonwealth Avenue, Boston, MA 02215, USA
[14] Saint Petersburg State University, 7/9 Universitetskaya nab., 199034 St. Petersburg, Russia
[15] Mullard Space Science Laboratory, University College London, Holmbury St Mary, Dorking, Surrey RH5 6NT, UK
[16] Instituto de Astrofísica de Andalucía–CSIC, Glorieta de la Astronomía s/n, 18008 Granada, Spain
[17] Department of Physics and Astronomy, 20014 University of Turku, Finland
[18] Hiroshima Astrophysical Science Center, Hiroshima University, 1-3-1 Kagamiyama, Higashi-Hiroshima, Hiroshima 739-8526, Japan
[19] Finnish Centre for Astronomy with ESO, 20014 University of Turku, Finland
[20] Aalto University Metsähovi Radio Observatory, Metsähovintie 114, FI-02540 Kylmälä, Finland
[21] Crimean Astrophysical Observatory RAS, P/O Nauchny, 298409, Crimea†
[22] Pulkovo Observatory, St. Petersburg, 196140, Russia
[23] Instituto de Astrofísica de Andalucía, IAA-CSIC, Glorieta de la Astronomía s/n, 18008 Granada, Spain
[24] INAF Osservatorio Astronomico di Brera, Via E. Bianchi 46, 23807 Merate (LC), Italy
[25] Geological and Mining Institute of Spain (IGME-CSIC), Calle Ríos Rosas 23, E-28003, Madrid, Spain
[26] Institut de Radioastronomie Millimétrique, Avenida Divina Pastora, 7, Local 20, E-18012 Granada, Spain
[27] Max-Planck-Institut für Radioastronomie, Auf dem Hügel 69, D-53121 Bonn, Germany
[28] Section of Astrophysics, Astronomy & Mechanics, Department of Physics, National and Kapodistrian University of Athens, Panepistimiopolis Zografos 15784, Greece
[29] Center for Astrophysics—Harvard & Smithsonian, 60 Garden Street, Cambridge, MA 02138, USA
[30] Korea Astronomy and Space Science Institute, 776 Daedeok-daero, Yuseong-gu, Daejeon 34055, Republic of Korea
[31] University of Science and Technology, Korea, 217 Gajeong-ro, Yuseong-gu, Daejeon 34113, Republic of Korea
[32] Graduate School of Sciences, Tohoku University, Aoba-ku, 980-8578 Sendai, Japan
[33] Department of Physics, Graduate School of Advanced Science and Engineering, Hiroshima University Kagamiyama, 1-3-1 Higashi-Hiroshima, Hiroshima 739-8526, Japan

[34] Department of Physics, Tokyo Institute of Technology, 2-12-1 Ookayama, Meguro-ku, Tokyo 152-8551, Japan
[35] Hiroshima Astrophysical Science Center, Hiroshima University 1-3-1 Kagamiyama, Higashi-Hiroshima, Hiroshima 739-8526, Japan
[36] Core Research for Energetic Universe (Core-U), Hiroshima University, 1-3-1 Kagamiyama, Higashi-Hiroshima, Hiroshima 739-8526, Japan
[37] Astronomy Research Center, Chiba Institute of Technology 2-17-1 Tsudanuma, Narashino, Chiba 275-0016, Japan
[38] Institute of Astrophysics, Foundation for Research and Technology - Hellas, Voutes, 7110 Heraklion, Greece
[39] Department of Physics, University of Crete, 70013, Heraklion, Greece
[40] INAF Osservatorio Astronomico di Roma, Via Frascati 33, 00078 Monte Porzio Catone (RM), Italy
[41] INAF Osservatorio Astronomico di Cagliari, Via della Scienza 5, 09047 Selargius (CA), Italy
[42] Istituto Nazionale di Fisica Nucleare, Sezione di Pisa, Largo B. Pontecorvo 3, 56127 Pisa, Italy
[43] Dipartimento di Fisica, Universitá di Pisa, Largo B. Pontecorvo 3, 56127 Pisa, Italy
[44] Dipartimento di Matematica e Fisica, Universitá degli Studi Roma Tre, Via della Vasca Navale 84, 00146 Roma, Italy
[45] Istituto Nazionale di Fisica Nucleare, Sezione di Torino, Via Pietro Giuria 1, 10125 Torino, Italy
[46] Dipartimento di Fisica, Universitá degli Studi di Torino, Via Pietro Giuria 1, 10125 Torino, Italy
[47] INAF Osservatorio Astrofisico di Arcetri, Largo Enrico Fermi 5, 50125 Firenze, Italy
[48] Dipartimento di Fisica e Astronomia, Universitá degli Studi di Firenze, Via Sansone 1, 50019 Sesto Fiorentino (FI), Italy
[49] Istituto Nazionale di Fisica Nucleare, Sezione di Firenze, Via Sansone 1, 50019 Sesto Fiorentino (FI), Italy
[50] Istituto Nazionale di Fisica Nucleare, Sezione di Roma "Tor Vergata", Via della Ricerca Scientifica 1, 00133 Roma, Italy
[51] Department of Physics and Kavli Institute for Particle Astrophysics and Cosmology, Stanford University, Stanford, California 94305, USA
[52] Institut für Astronomie und Astrophysik, Universität Tübingen, Sand 1, 72076 Tübingen, Germany
[53] Astronomical Institute of the Czech Academy of Sciences, Boční II 1401/1, 14100 Praha 4, Czech Republic
[54] RIKEN Cluster for Pioneering Research, 2-1 Hirosawa, Wako, Saitama 351-0198, Japan
[55] f, Via del Fosso del Cavaliere 100, 00133 Roma, Italy
[56] NASA Goddard Space Flight Center, Greenbelt, MD 20771, USA
[57] Yamagata University,1-4-12 Kojirakawa-machi, Yamagata-shi 990-8560, Japan
[58] Osaka University, 1-1 Yamadaoka, Suita, Osaka 565-0871, Japan
[59] University of British Columbia, Vancouver, BC V6T 1Z4, Canada
[60] International Center for Hadron Astrophysics, Chiba University, Chiba 263-8522, Japan
[61] Department of Physics and Astronomy and Space Science Center, University of New Hampshire, Durham, NH 03824, USA
[62] Dipartimento di Fisica, Universitá degli Studi di Roma "Tor Vergata", Via della Ricerca Scientifica 1, 00133 Roma, Italy
[63] Dipartimento di Fisica, Universitá degli Studi di Roma "La Sapienza", Piazzale Aldo Moro 5, 00185 Roma, Italy
[64] Istituto Nazionale di Fisica Nucleare, Sezione di Napoli, Strada Comunale Cinthia, 80126 Napoli, Italy
[65] Université de Strasbourg, CNRS, Observatoire Astronomique de Strasbourg, UMR 7550, 67000 Strasbourg, France
[66] MIT Kavli Institute for Astrophysics and Space Research, Massachusetts Institute of Technology, 77 Massachusetts Avenue, Cambridge, MA 02139, USA
[67] Graduate School of Science, Division of Particle and Astrophysical Science, Nagoya University, Furo-cho, Chikusa-ku, Nagoya, Aichi 464-8602, Japan
[68] Department of Physics, The University of Hong Kong, Pokfulam, Hong Kong
[69] Department of Astronomy and Astrophysics, Pennsylvania State University, University Park, PA 16802, USA
[70] Université Grenoble Alpes, CNRS, IPAG, 38000 Grenoble, France
[71] Center for Astrophysics—Harvard & Smithsonian, 60 Garden St, Cambridge, MA 02138, USA
[72] Dipartimento di Fisica e Astronomia, Universitá degli Studi di Padova, Via Marzolo 8, 35131 Padova, Italy
[73] Anton Pannekoek Institute for Astronomy & GRAPPA, University of Amsterdam, Science Park 904, 1098 XH Amsterdam, The Netherlands
[74] Guangxi Key Laboratory for Relativistic Astrophysics, School of Physical Science and Technology, Guangxi University, Nanning 530004, People's Republic of China

Received 2024 May 21; revised 2024 June 26; accepted 2024 July 13; published 2024 October 3

Abstract

We present multiwavelength polarization measurements of the luminous blazar Mrk 501 over a 14 month period. The 2–8 keV X-ray polarization was measured with the Imaging X-ray Polarimetry Explorer (IXPE) with six 100 ks observations spanning from 2022 March to 2023 April. Each IXPE observation was accompanied by simultaneous X-ray data from NuSTAR, Swift/XRT, and/or XMM-Newton. Complementary optical–infrared polarization measurements were also available in the *B*, *V*, *R*, *I*, and *J* bands, as were radio polarization measurements from 4.85 GHz to 225.5 GHz. Among the first five IXPE observations, we did not find significant variability in the X-ray polarization degree and angle with IXPE. However, the most recent sixth observation found an elevated polarization degree at $>3\sigma$ above the average of the other five observations. The optical and radio measurements show no apparent correlations with the X-ray polarization properties. Throughout the six IXPE observations, the X-ray polarization degree remained higher than, or similar to, the *R*-band optical polarization degree, which remained higher than the radio value. This is consistent with the energy-stratified shock scenario proposed to explain the first two IXPE observations, in which the polarized X-ray, optical, and radio emission arises from different regions.

Unified Astronomy Thesaurus concepts: Blazars (164); Active galaxies (17); Black holes (162); Relativistic jets (1390); Spectropolarimetry (1973); Polarimetry (1278); X-ray active galactic nuclei (2035)

1. Introduction

Blazars are a class of radio-loud active galactic nucleus (AGN), featuring relativistic jets powered by accreting supermassive black holes, with one of the jets pointing within $\sim 10^{\circ}$ of our line of sight (e.g., Hovatta & Lindfors 2019). The strongly beamed jet emission dominates the spectral energy distribution (SED), making blazars prime targets for studying particle acceleration and the nonthermal

[†] While the AAS journals adhere to and respect UN resolutions regarding the designations of territories (available at http://www.un.org/press/en), it is our policy to use the affiliations provided by our authors on published articles.

Table 1
Details of Each IXPE Observation Studied in This Work

IXPE OBSID	Date	Exp (ks)	Net Count Rate (cts s^{-1})	MDP_{99} (%)	Other X-Ray Data[a]
01004501 (IXPE1)	2022-03-07	104	0.24	6.4	NuSTAR 60701032002 (20 ks)
01004601 (IXPE2)	2022-03-27	87	0.44	5.0	NuSTAR 60702062004 (20 ks)
01004701 (IXPE3)	2022-07-09	98	0.21	7.5	Swift/XRT 00011184[b] (0.9 ks)
02004601 (IXPE4)	2023-02-12	95	0.12	9.5	XMM 0902111901 (14 ks)
02004501 (IXPE5)	2023-03-19	102	0.14	8.4	XMM 0902112201 (9 ks)
02004701 (IXPE6)	2023-04-16	94	0.15	8.5	Swift/XRT 00015411 (1.1 ks)

Notes. The net count rates shown here are the average background-subtracted 2–8 keV count rate per second. The Minimum Detectable Polarization at 99% confidence, MDP_{99}, is defined in Section 3.2.
[a] All IXPE observations reported here also have Swift XRT and UVOT coverage.
[b] XMM observed Mrk 501 simultaneously with IXPE, but XMM OBSID 0902110701 suffered from significant background flaring and was not included in this analysis.

emission mechanisms that occur in the jets (see, e.g., Blandford et al. 2019).

The advent of the Imaging X-ray Polarimetry Explorer (IXPE; Weisskopf et al. 2022) has enabled X-ray polarization measurements of blazars, which inform us about the magnetic field geometry during periods of efficient particle acceleration in the jets (Zhang & Böttcher 2013; Liodakis et al. 2019; Zhang et al. 2019; Peirson et al. 2022). The first IXPE observation of a blazar confirmed Mrk 501 to be linearly polarized at photon energies of 2–8 keV, with a polarization degree (PD) of ∼10%, several times the concurrent values at optical and radio wavelengths, with an electric vector polarization angle (PA) parallel to the jet axis on the sky (Liodakis et al. 2022). The initial results were interpreted in terms of synchrotron radiation arising from a shock-accelerated electron population that becomes energy-stratified due to radiative cooling. The electrons propagate away from the shock front, radiating at optical and radio wavelengths, with the PD decreasing as they encounter larger, and likely increasingly turbulent, regions of the jet flow.

Following Mrk 501, observations of similar blazars with the peaks of their synchrotron SEDs at ultraviolet or X-ray frequencies[75]—namely Mrk 421 (Di Gesu et al. 2022b, 2023; Kim et al. 2024), PG 1553+113 (Middei et al. 2023), 1ES 0229+20 (Ehlert et al. 2023), 1ES 1959+65 (Errando et al. 2024), and PKS 2155-304 (Kouch et al. 2024)—have provided further evidence supporting the shock-accelerated energy-stratified scenario.

Since the first two Mrk 501 observations in 2022 March, IXPE has obtained additional observations of the source accompanied by concurrent multiwavelength data, including one in 2022 July (Lisalda et al. 2024) and three more in 2023. Here, we present the analysis of the three 2023 observations and compare them to the three 2022 observations to provide the first long-term analysis of a blazar's X-ray polarimetric properties. Section 2 describes all of our multiwavelength polarization observations, and in Section 3, we discuss the X-ray polarimetric and spectroscopic data analyses. In Section 4, we analyze the long-term polarimetric behavior. We draw our conclusions in Section 5. The uncertainties reported in this work are at the 68% confidence interval (1σ) unless stated otherwise.

[75] Mrk 501 is an HSP source, defined as $\nu_{syn} > 10^{15}$ Hz (Ajello et al. 2020).

2. Data

2.1. IXPE Data

IXPE targeted Mrk 501 three times in 2023, following three pointings in 2022, all with exposure times of ∼100 ks (see Table 1 for details). For these observations, we first apply the background screening criteria of Di Marco et al. (2023) to the publicly available pipeline-processed level 2 events to remove background events. We then extract the polarization cube with the PCUBE algorithm, using the XPBIN function of IXPEOBSSIM,[76] with a 1′ radius source region centered at the source position. For each observation, a background polarization cube was also extracted from an annulus with 2.′5 and 5′ inner and outer radii, with the same center as the source position. Section 3 describes the procedures followed to generate the *I*, *Q*, and *U* Stokes parameters from the extracted IXPE data.

For each OBSID, spectra files were extracted using XSELECT, with the same source and background regions. For the spectral response functions, we used the 20240125 version of the IXPE CALDB, with the event weighing algorithm, using an elongation-normalized parameter of $\alpha^{0.75}$. We also accounted for the vignetting and aperture corrections to the auxiliary response functions using IXPECALCARF within the HEASARC FTOOLS (NASA High Energy Astrophysics Science Archive Research Center (HEASARC) 2014). While the IXPE observations for pointed sources generally place the target at the optical axis of the mirror modules, small offsets on the scale of ∼1′ are expected, due to IXPE's boom-drift correction and dithering effects. These effects were taken into account using IXPE's level 2 attitude files when deriving the vignetting and aperture corrections. We group the total flux density (Stokes *I*) spectra with a minimum of 25 counts per bin. The *Q* and *U* spectra were binned with a constant five channels (0.2 keV) per bin.

IXPE also observed Mrk 501 three times in 2022 (see Table 1). We reprocessed and extracted PCUBE and spectra for the 2022 observations similar to how we processed the 2023 observations. One distinction is that for the first two IXPE observations in 2022, we used a fixed off-axis angle of 2.′73 to calculate the vignetting and aperture correction to the response functions, instead of using the attitude files. This is motivated by a correction in the IXPE optical axis relative to the star trackers, which took place on 2022 June 7. For the remainder of

[76] Version 31.0.1, with instrument response function v13; see https://github.com/lucabaldini/ixpeobssim.

the paper, we refer to the six IXPE observations in their chronological order (see Table 1) as IXPE1 through IXPE6.

2.2. Ancillary X-Ray Data

To supplement the IXPE observations, we make use of the contemporary ancillary X-ray data from NuSTAR and XMM-Newton, when available; see Table 1. Mrk 501 is one of the targets in the list of Fermi-LAT "sources of interest," with extensive monitoring by the Neil Gehrels Swift Observatory X-Ray Telescope (XRT; Stroh & Falcone 2013). For the remaining IXPE observations without contemporary NuSTAR or XMM-Newton data, we make use of Swift/XRT data obtained during the IXPE pointing. The ancillary X-ray data are used for the spectral and spectral-polarimetric analysis described in Section 3. Additionally, photometric measurements from the Swift Ultraviolet/Optical Telescope (UVOT) were also included in our analysis. For NuSTAR and Swift/XRT and UVOT data, HEASOFT 6.31.1 was used for data reduction and extraction. For XRT, the Windowed Timing (WT)–mode spectra were extracted using a circular region with a 47″ radius, with backgrounds accounted for with time-dependent WT background files. For the Photon Counting–mode observations, the spectra were extracted following the procedures described in Middei et al. (2022; see their Section 2). For NuSTAR, we extracted spectra from both focal plane modules with a 90″ radius source aperture and a background annulus with 150″ and 220″ inner and outer radii, respectively. For XMM-Newton, XMMSAS version 20.0.0 was used for data reduction and spectral extraction of the EPIC-PN data. Background flares were screened and filtered using a 3σ clipping algorithm. The source and background spectra were extracted from the timing-mode data with a source region of 20 detector rows and a source-free region between $3 \leqslant \mathrm{RAWX} \leqslant 5$.

2.3. Multiwavelength Observations

The multiwavelength observations contemporaneous with the three IXPE pointings in 2022 are described in detail in Liodakis et al. (2022) and Lisalda et al. (2024). The details of the analysis of the data from the different telescopes can be found there as well. Here, we provide a short description and present the multiwavelength observations taken around the 2023 IXPE observation dates.

Similar to the previous IXPE sessions, a number of telescopes operating across the electromagnetic spectrum provided contemporaneous data. Here, we focus on the radio and optical regimes. For a discussion on the very-high-energy γ-ray behavior of Mrk 501 during the first three IXPE observations, see MAGIC Collaboration et al. (2024). At radio wavelengths, those telescopes included the Effelsberg 100 m antenna, the IRAM 30 m telescope, the Korean VLBI Network (KVN), and the Submillimeter Array (SMA; Ho et al. 2004). These facilities provide coverage from 4.85 to 225.5 GHz. Effelsberg observations at 4.85, 10.45, and 17 GHz were obtained as part of the Monitoring the Stokes Q, U, I, and V Emission of AGN jets in Radio program (Kraus et al. 2003; Myserlis et al. 2018). Observations at 86 GHz with the IRAM 30 m telescope were taken as part of the Polarimetric Monitoring of AGN at Millimeter Wavelengths (POLAMI) project[77] (Agudo et al. 2018a, 2018b; Thum et al. 2018). The KVN observations used the Yonsei and Tamna antennas in single-dish mode to provide observations at 22, 43, 86, and 129 GHz (Kang et al. 2015). Finally, 225.5 GHz observations were taken within the SMA Monitoring of AGNs with Polarization program (I. Myserlis et al. 2024, in preparation). All of the radio observations are shown in the appendix (Figure A1). The source exhibited a low degree of polarization (<4%) for the entire monitoring period, with a roughly constant PA fluctuating about an average of $\mathrm{PA_{Rad}} = 157^\circ \pm 3^\circ$ at 225.5 GHz to $\mathrm{PA_{Rad}} = 170^\circ \pm 1^\circ$ at 4.85 GHz. We note the radio polarimetry measurements utilized in this work were all obtained with either single-dish observatories or radio telescope arrays in single-dish modes. The observed radio emission is thus dominated by the unresolved blazar jet emission and the fluxes and polarization measurements are not affected by the different aperture sizes between radio observatories. However, radio observations at higher frequencies tend to have less significant Faraday depolarization (Burn 1966), therefore we primarily consider the high-frequency polarization measurements (see Table 2).

In the optical and infrared (IR) regime, Mrk 501 was observed using the Calar Alto Observatory's 2.2 m telescope, the Haleakala Observatory's T60, the KANATA telescope, LX-200 operated by St. Petersburg State University, the Nordic Optical Telescope (NOT), the 1.8 m Perkins Telescope Observatory (PTO; Boston University), and the Sierra Nevada Observatory (SNO) T90 telescope. The Calar Alto observations used the Calar Alto Faint Object Spectrograph to provide R-band observations. T60 used the DiPol-2 polarimeter (Piirola et al. 2014, 2020), which can simultaneously measure the PD in the B, V, and R bands. LX-200 provided R-band polarimetry and B, V, R, and I photometry. The Hiroshima Optical and Near-InfraRed camera[78] at the KANATA telescope (Kawabata et al. 1999; Akitaya et al. 2014) can simultaneously measure polarization at multiple optical/IR bands; it provided R- and J-band observations. NOT used the Alhambra Faint Object Spectrograph and Camera (ALFOSC) and the Tuorla Observatory's semi-automatic data reduction pipeline (Hovatta et al. 2016; Nilsson et al. 2018) for B, V, R, and I observations. PTO used the PRISM camera[79] for polarimetric (R) and photometric (B, V, R, and I) observations. The T90 observations at SNO were performed with a set of polarized filters in R band. Several observations were obtained within a single night, which were then binned using a weighted average. All of the optical and IR observations are shown to the right of Figure A1.

Unpolarized flux from the host galaxy of Mrk 501 contributes significantly to the optical/IR emission. This leads to depolarization, which we correct by subtracting the host galaxy flux within a given aperture (Nilsson et al. 2007), following Hovatta et al. (2016). Only the R-band observations are corrected, since we lack a model for the host galaxy light for the other bands. Instrumental limitations prevent us from correcting the T60 observations. All the other R-band observations have been corrected for host galaxy depolarization.

We were not able to obtain J-band observations simultaneous with the IXPE pointings; however, the two available observations between the fourth and fifth IXPE exposures appear consistent with the optical bands. The observed PD is

[77] http://polami.iaa.es/

[78] http://hasc.hiroshima-u.ac.jp/instruments/honir/filters-e.html

[79] https://www.bu.edu/prism/

Table 2
Summary for the Multiwavelength Data Reported in This Work

Observation	Optical–IR	Radio (GHz)	PD_{Opt} (*R*)	PA_{Opt}	PD_{radio} (86, 225.5 GHz)	PA_{Radio} (86, 225.5 GHz)
	(1)	(2)	(3)	(4)	(5)	(6)
IXPE1	*V*, **B**, *R, I, J*	86	6.6 ± 0.4	110 ± 5	1.5 ± 0.5, -	148 ± 10, -
IXPE2	*V*, **B**, *R, I, J, H, K*	N/A	4.7 ± 0.3	120 ± 3	–, –	–, –
IXPE3	*V*, **B**, *R, I, J, H, K*	86, 225.5	2.7 ± 0.5	109 ± 5	1.5 ± 0.3, 1.3 ± 0.3	144 ± 5, 130 ± 3
IXPE4	*V*, **B**, *R, I*, J	4.85, 10.45, 17, 86, 225.5	6.6 ± 0.9	150 ± 4	3.2 ± 0.6, 2.9 ± 0.5	176 ± 3, 162 ± 2
IXPE5	*V*, **B**, *R, I, J*	4.85, 10.45, 17, 22, 43, 86, 225.5	6.1 ± 0.7.	125 ± 3	–, 1.75 ± 0.2	–, 154 ± 3
IXPE6	V, *R,* I, J	4.85, 10.45, 17, 22, 43, 86, 225.5	5.9 ± 1.5.	108 ± 6	–, 3.3 ± 0.4	–, 156 ± 2

Note. Column (1): the available optical to IR bands. Column (2): the available radio bands in GHz. The italicized fonts denote bands for which both polarimetric and photometric measurements were available. Bands with only polarimetric measurements are shown in boldface. Columns (3) and (4): the host-galaxy-subtracted polarimetric measurement results for the *R* band. Columns (5) and (6): for radio polarimetric measurements, the polarimetric measurements from the higher-frequency bands, 86 GHz and 225.5 GHz. See Section 2.3 for details. From columns (3) to (6), the PD values are shown in percent and the PA values are shown in degrees.

consistent within uncertainties in all optical/IR bands and appears to vary in tandem. The intrinsic *R*-band PD (PD_{opt}, hereafter) varies from about 1.6% to ∼9%, with a median of $6.6\% \pm 1.9\%$. The PA (PA_{Opt}, hereafter) fluctuates around the jet axis position angle on the plane of the sky ($120° \pm 12°$; Weaver et al. 2022) from ∼100° to ∼150°, with a median of $133° \pm 14°$. A summary of the multiwavelength observations is provided in Table 2.

3. Analysis

3.1. Spectropolarimetry

For the spectropolarimetric analysis, we combine a log-parabola spectrum (Massaro et al. 2004) with a multiplicative model that applies a constant polarization, POLCONST. The model used in XSPEC can be written as follows:

$$\text{const} \times \text{TBabs} \times \text{polconst} \times \text{logpar}.$$

The CONST component accounts for the instrumental normalization. The POLCONST component includes two parameters: the polarization degree PD_X and the polarization angle PA_X. The log-parabolic model is defined as $F(E) = K(E/E_{pivot})^{-(\alpha+\beta\log(E/E_{pivot}))}$. The parameters α, β, and E_{pivot} define the energy-dependent power-law index of the spectrum, and K represents the normalization. E_{pivot} is a constant for optimal fitting results in the log space, here fixed to 1 keV. The results of the analysis, including both IXPE and ancillary soft-X-ray data, are listed in Table 1. The XMM-Newton and Swift/XRT data were limited to 0.5–10 keV for the model fitting. For NuSTAR, the 3–30 keV data were used (higher-energy channels were not used, due to the limited signal-to-noise ratio). For spectral fitting, we used a Markov Chain Monte Carlo (MCMC) sampling approach with the Goodman–Weare algorithm and 500,000 steps. As a demonstration, we plot the spectra and the data/model ratio for IXPE6 in Figure 1. The *I, Q,* and *U* spectral plots for the other IXPE observations are shown in the Appendix in Figures A2 and A3. We also repeated the analysis using only the IXPE data, and found the results to be generally consistent with the analysis with the ancillary X-ray data.

The fitting parameters are listed in Table 3. For comparison, the PD and PA from the PCUBE analysis and the spectropolarimetric analysis are listed in Table 4 and shown in Figure 2. We also extracted time-averaged IXPE spectra by merging event lists from all six observations. The source and background spectra were generated from merging events in the source and background regions for each observation, respectively. The ancillary response function was calculated with the IXPECALCARF script in a similar manner as for each observation.

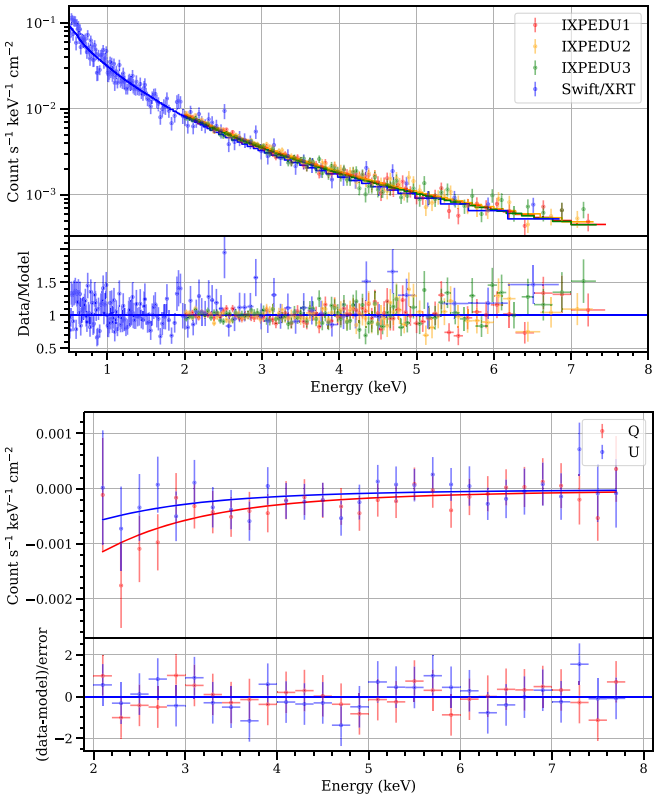

Figure 1. Spectra during IXPE6 of Mrk 501 with ancillary X-ray data. The solid lines are the best-fit models. Top: Swift/XRT and IXPE total flux density spectra. Bottom: IXPE *Q* and *U* spectra for DU1.

3.2. Model-independent Polarimetry with IXPE

Here, we describe the results from the polarization cube analysis, which calculates the X-ray PD (PD_X) and PA (PA_X)

Table 3
Spectral-polarimetric Results with IXPE and Ancillary X-Ray Data for Each ObsID, Including the Fitting Statistics and dofs, Log-parabolic Model Parameters α, β, and Normalization (Norm), and the PD and PA

IXPE Observation	χ^2/dof	α	β	Norm	PD (%)	PA (deg)
IXPE1	1285.46 / 1274	1.75 ± 0.04	0.36 ± 0.02	0.043 ± 0.001	9.8 ± 1.7	-44 ± 5
IXPE2	1654.83 / 1480	1.50 ± 0.03	0.40 ± 0.02	0.066 ± 0.001	10.3 ± 1.4	-65 ± 4
IXPE3	559.2 / 643	1.99 ± 0.02	0.36 ± 0.03	0.053 ± 0.001	6.9 ± 1.8	-46 ± 8
IXPE4	582.1 / 577	2.28 ± 0.00	0.10 ± 0.01	0.037 ± 0.000	9.0 ± 2.4	-70 ± 8
IXPE5	594.88 / 589	2.27 ± 0.01	0.03 ± 0.01	0.041 ± 0.000	6.0 ± 2.1	-73 ± 11
IXPE6	603.62 / 599	2.15 ± 0.02	0.2 ± 0.03	0.041 ± 0.001	18.5 ± 2.2	-77 ± 3

Note. The uncertainties quoted here are for 68% confidence intervals.

Table 4
Comparison between Polarization Measurements with PCUBE Analysis and Spectral-polarimetric Analysis with and without Ancillary X-Ray Data

	PCUBE		Spectropolarimetry (All)		Spectropolarimetry (IXPE Only)	
	PD (%)	PA (deg)	PD (%)	PA (deg)	PD (%)	PA (deg)
IXPE1	10.1 ± 2.1	-53 ± 6	9.8 ± 1.7	-44 ± 5	9.0 ± 2.6	-44 ± 8
IXPE2	11.4 ± 1.7	-64 ± 4	10.3 ± 1.4	-65 ± 4	9.4 ± 2.0	-64 ± 6
IXPE3	5.9 ± 2.3	-40 ± 11	6.9 ± 1.8	-46 ± 8	6.9 ± 2.9	-48 ± 12
IXPE4	9.9 ± 3.2	-75 ± 9	9.0 ± 2.4	-70 ± 8	9 ± 4	-71 ± 16
IXPE5	6.7 ± 2.8	-84 ± 12	6.0 ± 2.1	-73 ± 11	5.9 ± 3.4	-72 ± 17
IXPE6	15.3 ± 2.8	-82 ± 5	18.5 ± 2.2	-77 ± 3	16.3 ± 3.4	-76 ± 6
Combined	8.9 ± 1.0	-65 ± 3	...	...	8.7 ± 1.2	-62 ± 4

using the Stokes parameters I, Q, and U for all of the events within the source extraction region, where $\mathrm{PD_X} = \sqrt{(Q/I)^2 + (U/I)^2}$ and $\mathrm{PA_X} = 0.5 \arctan(U/Q)$ (Kislat et al. 2015). Background subtraction was accomplished by subtracting the sums of the Stokes parameters in the background region from those in the source region. We report the model-independent polarization measurement events in the 2–8 keV range in Table 4. The minimum detectable polarization at the 99% confidence interval ($\mathrm{MDP_{99}}$), defined as $\mathrm{MDP_{99}} \approx 4.29/(\sqrt{C_s}\langle\mu\rangle)$, is dependent on the mean count-weighted modulation factor $\langle\mu\rangle$ and the total source photon counts C_s. The 2–8 keV $\mathrm{MDP_{99}}$ is listed in Table 1. To test the feasibility of energy-resolved polarimetry, we divided IXPE6 into two energy bins covering the range 2–4 keV and 4–8 keV. IXPE6 has the highest 2–8 keV PD among all IXPE observations at $15.3\% \pm 2.8\%$, with $\mathrm{MDP_{99}} = 8.5\%$. However, $\mathrm{MDP_{99}}$ over 4–8 keV increases to 21%, and we did not find significant polarization detection in this high-energy bin. Similar results with 4–8 keV PD $<$ $\mathrm{MDP_{99}}$ were found for the other IXPE observations. Therefore, we do not include energy-resolved analysis in this work.

In summary, we detected polarization at $>3\sigma$ significance for the first two and the last IXPE observations, both with the spectropolarimetric or PCUBE analysis. The detection significance of the other three observations was slightly less than 3σ.

3.3. Polarization Variability

For individual IXPE observations, we investigated whether the polarization varied on various timescales within each observation. This is motivated by the recent observations of another high-synchrotron-peaked (HSP) blazar, Mrk 421, which showed a rotation in the PA during one of its observations (Di Gesu et al. 2023). The details of the timing analysis are described in Section 2.2 of Kim et al. (2024). In short, for each observation, the data were divided into N bins with identical widths in time, where N ranged from 2 to 15. For a 100 ks observation, this means that the time in each bin ranges from 50 to 6.7 ks. For each binning scheme, the normalized Stokes parameters Q and U were calculated. The distributions of Q and U as a function of time were then compared to the assumption that Q and U are constant over time. See Figure 3 for an example. For each bin, the comparison was done with a χ^2 test. We found that all six observations have Q and U distributions consistent with the time-independent assumption (i.e., the null hypothesis $P_{\mathrm{Null}} > 1\%$; see Figure 3), suggesting that the 2–8 keV polarization of Mrk 501 did not vary significantly during each of the IXPE observations reported here.

4. Long-term Variability

4.1. X-Ray

We first show the spectral properties computed from the 167 Swift/XRT observations described in Section 2 and plotted in Figure 4. The fluxes were obtained by fitting the 0.3–10 keV Swift/XRT data with a log-parabola model with a pivotal energy set to 1 keV. Photo-electric absorption from Galactic gas with a column density $N_{\mathrm{H}} = 1.69 \times 10^{20}\ \mathrm{cm^2}$ was included in the spectral fits. During the time between IXPE1 and IXPE6, the Swift/XRT X-ray fluxes ranged between $-10.38 < \log F_{0.3-10\ \mathrm{keV}} < -9.58$ ($\mathrm{erg\ s^{-1}\ cm^{-2}}$), with the flux peaking at the first two IXPE observations, then gradually declining into a relatively quiescent state seen in the last three observations. The log-parabola spectral parameters, α and β,

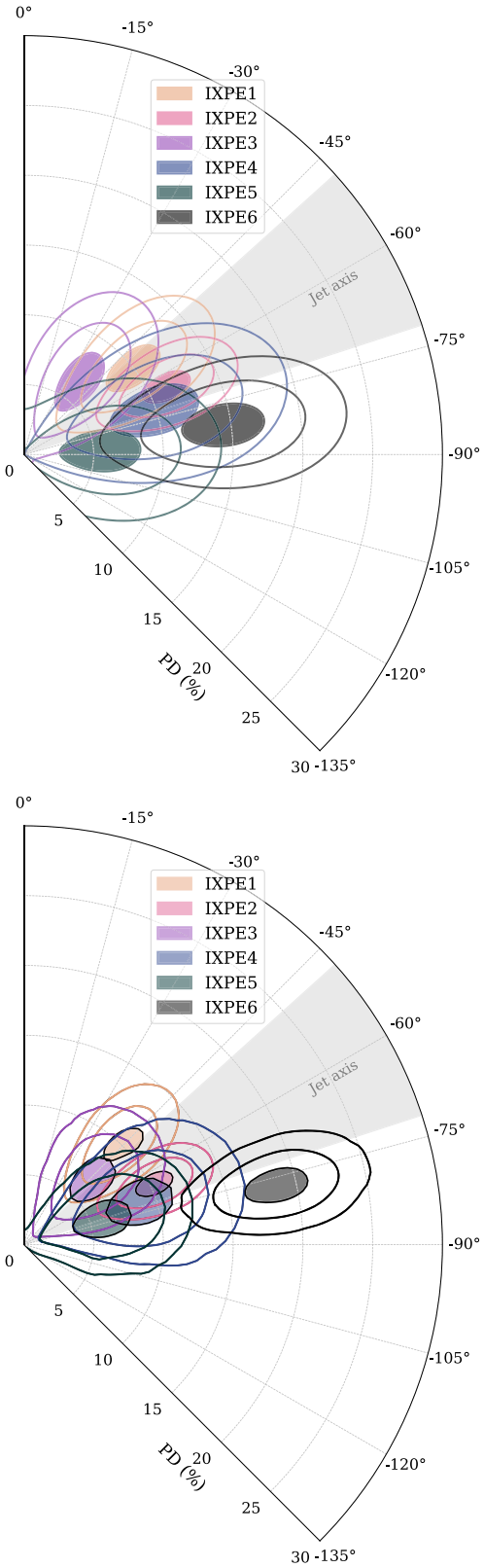

Figure 2. Polar plots displaying polarization measurements based on the model-independent PCUBE analysis (top). The contours represent the 1σ, 2σ, and 3σ uncertainties in PD_X and PA_X based on the Q, U error circles and their relations to PD_X and PA_X described in Section 3.2. The spectropolarimetric fitting results with IXPE and ancillary X-ray data analysis are shown in the bottom. The error contours are based on the MCMC sampling described in Section 3.1 within the 68%, 95%, and 99.7% ranges. The results obtained from these two independent methods are consistent with each other.

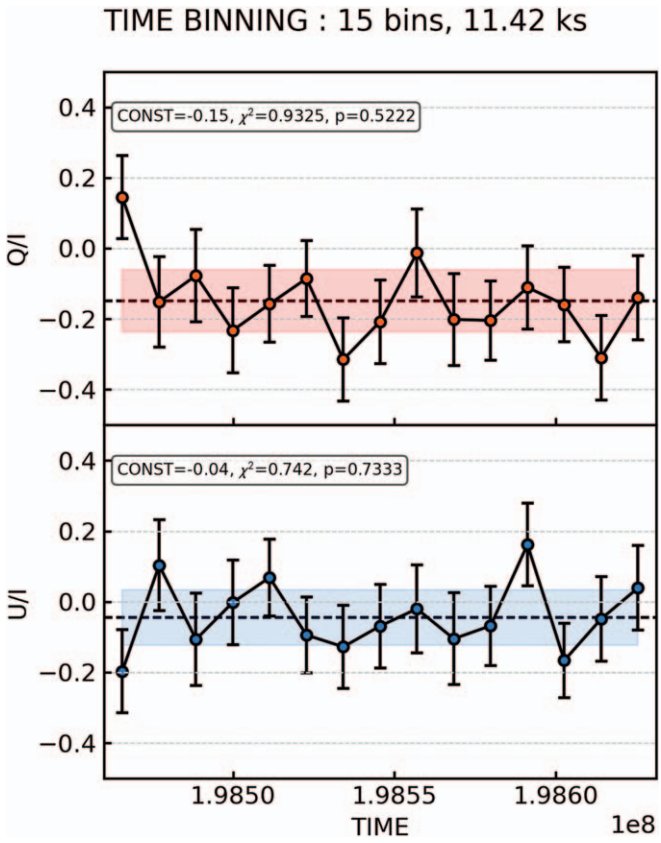

Figure 3. Top: light curves for the Stokes parameters Q and U for IXPE6; the dotted lines and the shaded regions represent the time-averaged values. Bottom: null-hypothesis probability ($P_{\rm Null}$) of the χ^2 test for the variability of Q and U for IXPE6. The green shaded area above the dashed line marks the region with $P_{\rm Null} > 1\%$. The dotted line represents the 3σ (99.73%) significance level. For the range of bin sizes explored here, we find no statistical evidence ($<3\sigma$) that Mrk 501 varied in either Q or U. Similar results were found for all six Mrk 501 IXPE observations discussed in this work.

and the hardness ratio—HR_{XRT} as (H−S)/(H+S), where H and S are Swift/XRT 2–10 keV and 0.5–2 keV fluxes, respectively—are also shown in Figure 4. Generally, Mrk 501 followed the typical "harder-when-brighter" behavior (e.g., Zhang et al. 2005). We also show the relation between the X-ray PD and IXPE 2–8 keV flux, hardness ratio (HR_{IXPE}, defined as (H−S)/(H+S), where S and H are IXPE fluxes between 2–4 and 4–8 keV, respectively), α, and β in Figure 5.

The first three IXPE observations were discussed in Liodakis et al. (2022) and Lisalda et al. (2024), who found Mrk 501 to have X-ray PAs roughly parallel to the radio jet axis. The X-ray emission was polarized at $PD_X \sim 10\%$ in the first two IXPE observations (Liodakis et al. 2022). The third IXPE observation formally had a PD that was slightly smaller, but still consistent with the first two observations within the uncertainties. During 2023, Mrk 501 entered a lower-flux state (Figure 4). The lower number of counts, softer spectra, and corresponding MDP_{99} resulted in only marginal detection of polarization during IXPE4 and IXPE5, while the position angle of polarization remained parallel to the jet axis within uncertainties. Intriguingly, the last 2023 observation (IXPE6) showed the highest PD_X since the launch of IXPE, while maintaining a similar PA within the uncertainties. The spectropolarimetric

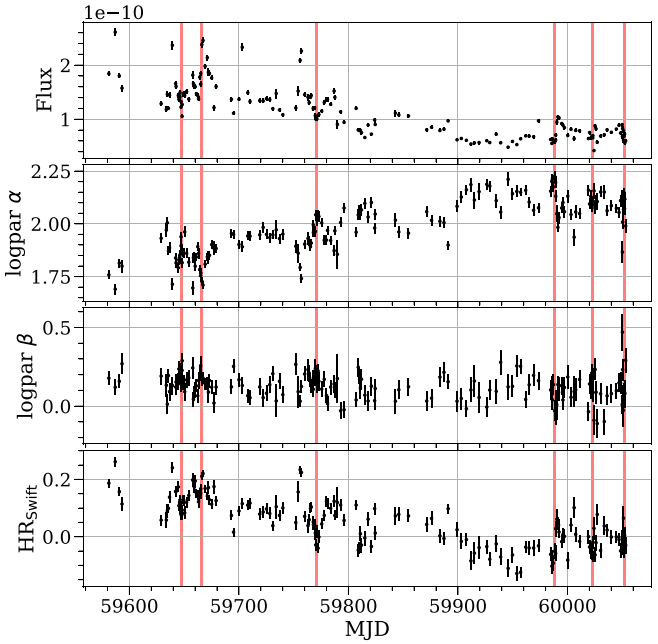

Figure 4. Swift/XRT X-ray spectral properties as a function of time in MJD. From top to bottom, the panels include the 2–8 keV flux in 10^{-10} erg s^{-1} cm^{-2}, the log-parabolic model parameters α and β, and the spectral hardness ratio, defined as (H−S)/(H+S), where H and S are Swift fluxes in the 2–10 keV and 0.5–2 keV bands, respectively. The dates of the IXPE observations are highlighted in red.

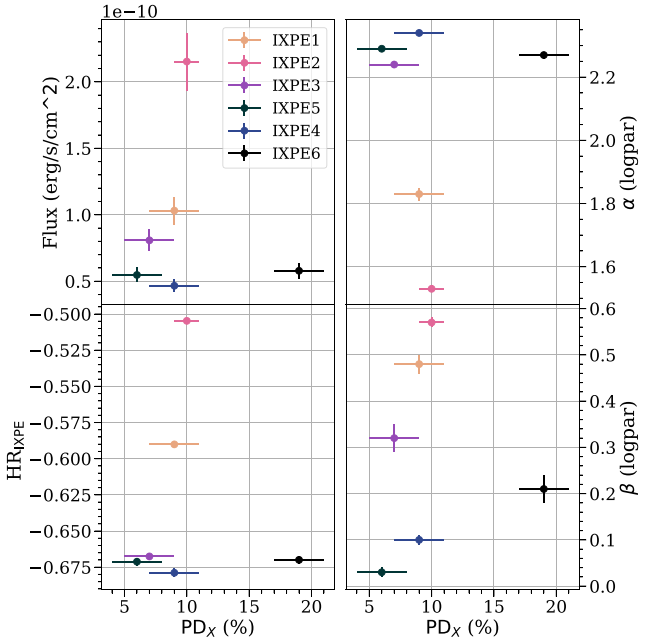

Figure 5. Various X-ray spectral properties as a function of the X-ray PD, including the IXPE 2–8 keV flux (top left), photon index α (top right), IXPE 2–4 and 4–8 keV hardness ratio (HR_{IXPE}, bottom left; see Section 4.1 for definitions), and spectral curvature (bottom right).

analyses suggest that IXPE6 is outside the 3σ uncertainty range compared with IXPE1 to IXPE3. To quantify the deviation of IXPE6 from the other five IXPE observations, we compare the PA and PD measurements of IXPE6 with the average of the other five observations with a χ^2 test. This is based on the assumption that the other five observations have similar PA and PD distributions (see Figure 2). The test has a result of $\chi^2 = 17.08$. In the two degree of freedom (dof) case, this corresponds to a p-value of 0.0002 ($>3\sigma$), rejecting the null hypothesis that the elevated PD for IXPE6 is simply due to statistical fluctuations.

We also explored whether the Stokes parameters of the last IXPE observation have a different distribution than the rest of the observations via two-sample, two-dimensional, Kolmogorov–Smirnov (K-S) tests (Peacock 1983). We calculated the K-S test between the Q and U parameters of each two pairs of IXPE observations. Most of the combinations have a very small p-value <0.05, rejecting the null hypothesis that their Stokes parameters have different distributions. This is not surprising, as the nonparametric statistics we tested would be dominated by unpolarized events that should have insignificant differences between observations due to the high X-ray PD. Despite the substantial increase in PD for IXPE6, we find no strong correlation between PD and other spectral properties of IXPE, as demonstrated in Figure 5.

4.2. Multiwavelength Properties

We plot the multiwavelength flux variability spanning the time between the IXPE1 and IXPE6 observations in Figure 6, including X-ray fluxes in the IXPE bandpass (2–8 keV) from 167 Swift/XRT exposures taken between 2022 January 1 and 2023 April 15. The IXPE fluxes derived from the best-fit models are also shown in the same plot, as are the fluxes in the optical R band and radio 86 and 225 GHz bands. The R-band observations were host-galaxy-subtracted. We also show the polarization properties measured by IXPE, the R band, 225 GHz, and 86 GHz in Figure 7, including the time dependence of the PD, the X-ray to optical PD ratio, and the PA.

In Figure 8, we display the broadband SED of Mrk 501 during all six IXPE sessions, including the X-ray spectra from IXPE and ancillary data sets, as well as Swift/UVOT, optical, and radio photometry. For each observation, we have also calculated the peak energy of the best-fit log-parabolic model (Massaro et al. 2004) used in the spectral-polarimetry analysis, with $E_{\rm peak} = E_{\rm pivot}\, 10^{(2-\alpha)/(2\beta)}$.

In general, we find the IXPE fluxes to be within the average fluctuations typically observed from this target (e.g., see Liodakis et al. 2022). This would suggest that all of the IXPE observations of Mrk 501 were taken in average/quiescent state. Similarly, neither the radio nor optical observations show any substantial deviation from the long-term average behavior of the source (see Figure 8). For the last IXPE observation (IXPE6), the PD_X value is elevated above 3σ of the average value of the other five IXPE observations. Other than the elevated PD_X, we do not find any substantial differences for IXPE6 from the other observations, including the multiwavelength PDs and PAs, X-ray spectral shapes, and multiwavelength fluxes.

We find no apparent correlations in the time dependence of the flux, PD, or PA values at different wavelengths, as shown in Figures 6 and 7, which is in broad agreement with the energy-stratified shock scenario discussed in Liodakis et al. (2022), wherein the polarized emission in the optical and radio bands originates from regions larger than the region emitting polarized X-ray emission. We also find the X-ray PD (PD_X) to be higher, or (at one epoch) similar to, the R-band

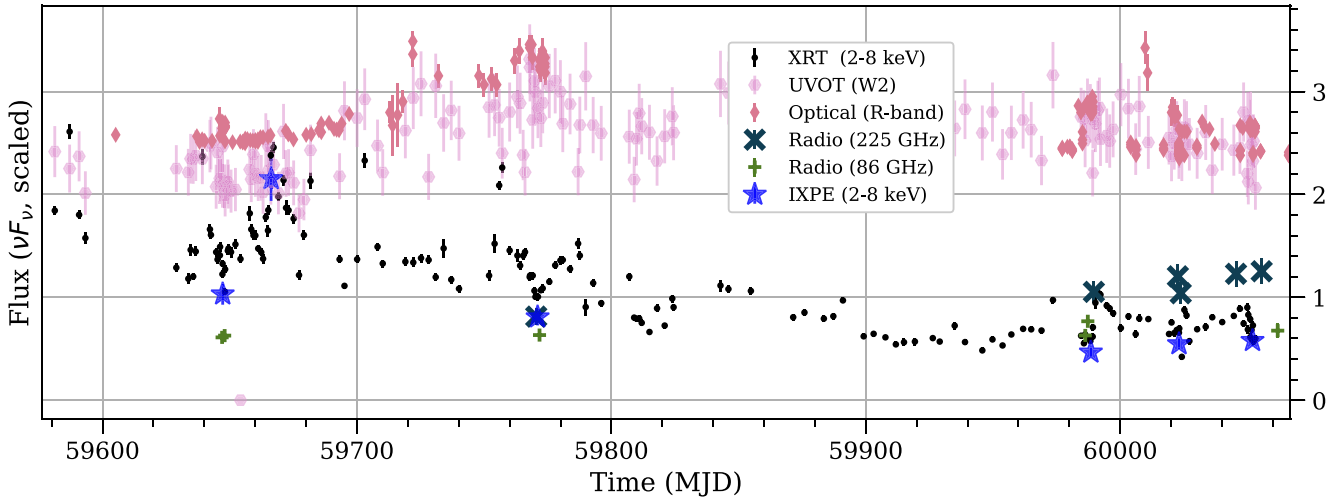

Figure 6. Multiwavelength Mrk 501 variability of fluxes spanning the six IXPE observations. The fluxes in each band are normalized by 10^{-10}, 10^{-11}, 10^{-11}, and 10^{-12} erg s^{-1} cm^{2} for the X-ray, UV, optical R, and radio bands, respectively.

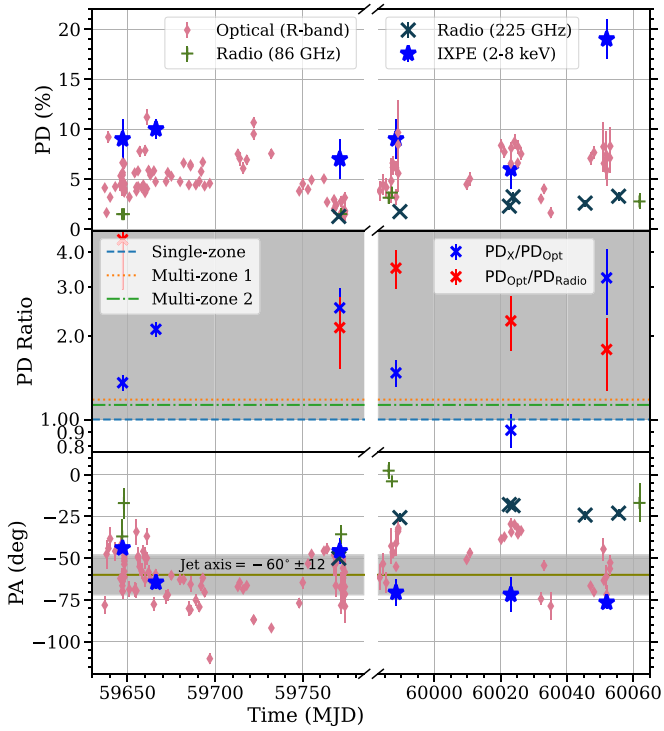

Figure 7. Multiwavelength variability of Mrk 501: PD (top), PD ratios between different bands (middle), and PA (bottom), spanning the six IXPE observations. For the middle panel, the PD ratios shown here are the X-ray to optical *R*-band PD ratios (PD_X/PD_{Opt}) and the optical *R*-band to radio 225 GHz (except for IXPE1, where only the 86 GHz PD measurement was available) PD ratios (PD_{Opt}/PD_{radio}). For the PD_X/PD_{Opt} in the middle panel, we also marked the regions expected based on energy-stratified shocks in gray. The expected values from a single-zone jet model (Di Gesu et al. 2022a) and two turbulent multizone jet models, including Marscher (2014, Multizone 1) and Peirson & Romani (2019, Multizone 2), are also shown.

PD (PD_{opt}), while the *R*-band PD is higher than the radio PD. This is again consistent with the energy-stratified shock scenario. For IXPE5, PD_{opt} appears to be marginally higher than PD_X, with $PD_X/PD_{opt} = 0.92 \pm 0.12$ (1σ uncertainty). Note that IXPE5 has the second-lowest flux and the softest X-ray spectrum (see Figure 5). Therefore, given the uncertainty of the X-ray PD, IXPE5 is still statistically consistent with $PD_X/PD_{opt} \geqslant 1$.

Spanning the six IXPE observations, the X-ray PD values are generally higher than PD_{opt}, and PD_{opt} is higher than PD_{rad}. This is consistent with the energy-stratified shock scenario, in which the location of the X-ray emission region is closer to the shock front than that of the longer-wavelength emission. The lower PD_X we see in IXPE4 and IXPE5 might be attributed to the change of the spectral curvature, which can be connected to a decrease in the magnetic field strength (e.g., MAGIC Collaboration et al. 2024). Such a decrease would lower the flux and peak frequency of the SED and weaken the radiative energy losses. The former effect increases the spectral curvature, while the latter increases the volume of the emitting region, thereby lowering its degree of polarization. Alternatively, increased turbulence could also decrease the uniformity of the magnetic field and hence the PD. However, in this case, one would not expect the curvature of the SED to increase. Detailed SED modeling of our observations, planned in a follow-up study, can further elucidate the physical processes in the X-ray-emitting region of the jet.

We note that the detected X-ray PD fluctuates between ∼10% and 20%, far lower than the synchrotron limit (e.g., Rybicki & Lightman 1979). This implies that the observed X-ray emission originates from at least a partially turbulent emission region that is close to the site of particle acceleration. This shock-plus-turbulence scenario naturally explains why the elevated PD during IXPE6 was only seen in X-rays. We also note the lower PD_{opt} values measured in IXPE4 and IXPE5 are still within the 3σ uncertainty of the average among all six observations or of the 2022 IXPE observations with higher PD. A variety of physical mechanisms could drive the limited fluctuations we see among the six IXPE observations. However, based on the overall trend of the elevated PD in X-rays compared to longer wavelengths, we argue that these six IXPE observations are generally consistent with the energy-stratified shock scenario, with a highly turbulent magnetic field structure beyond the shock front.

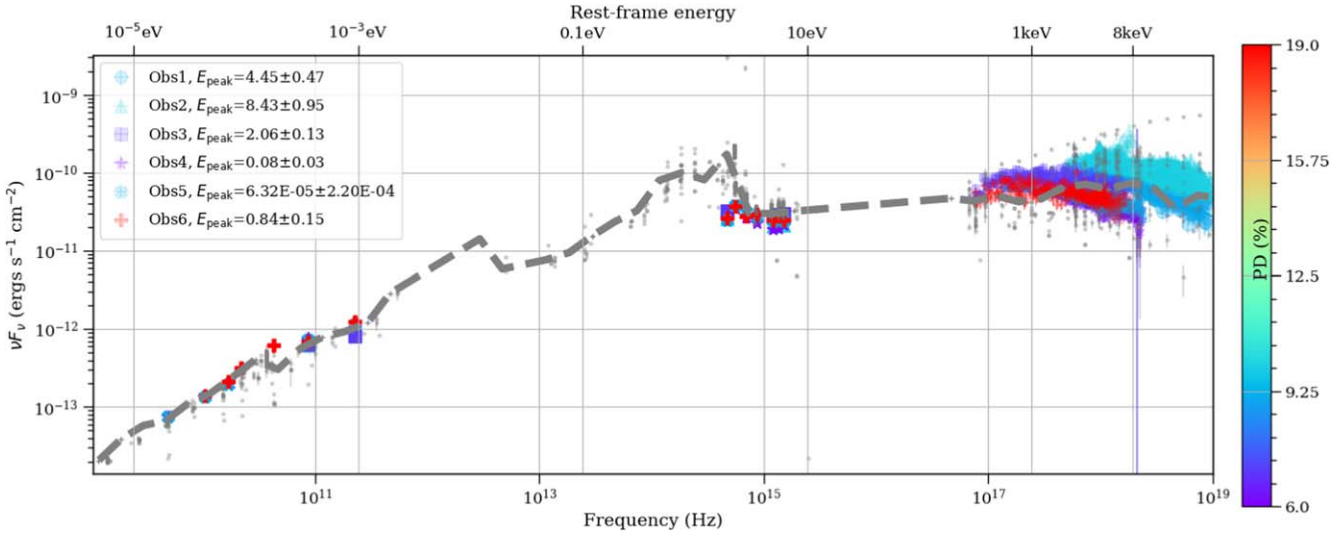

Figure 8. Broadband SED of Mrk 501, with best-fit log-parabolic model from X-ray spectropolarimetric fitting, superposed on archival data (gray points) from the SSDC SED Builder (Tramacere et al. 2009; https://tools.ssdc.asi.it/SED/). For comparison, we also display the archival data binned by 0.2 dex in log frequency as a dashed gray line. The vertical color bar represents the PD of each observation.

5. Conclusion

We have presented three additional IXPE observations of the archetypal HSP blazar Mrk 501 obtained in 2023. Combined with the three 2022 observations, our data set constitutes the first long-term X-ray polarization light curve from a blazar. All of our observations were supplemented with simultaneous multiwavelength campaigns. During the 14 month span of our observations, the source was in an average-to-quiescent flux state across different wavelengths, as well as in a typical radio, IR, and optical polarization state. For Mrk 501, the X-ray PD values were found to be generally higher than those in other wavelengths, with occasional drops in the X-ray PD to a level consistent with the optical PD. The higher X-ray PD measurements compared to those in other wavelengths are common among IXPE-observed HSP blazars (e.g., Di Gesu et al. 2022b; Middei et al. 2023; Ehlert et al. 2023; Errando et al. 2024; Kim et al. 2024), as are the fluctuations in the X-ray to optical PD ratio (Errando et al. 2024). These provide further evidence for shock-accelerated electron populations that become energy-stratified as they advect downstream from the shock front inside a turbulent plasma. For Mrk 501, the PA at all wavelengths fluctuates only modestly around the jet axis on the plane of the sky, even when the PD changes by a factor of 2. This is also common among IXPE-observed HSP blazars, implying that the physics of HSP blazars is essentially the same throughout the subclass of AGNs, even though Mrk 421 has shown large rotations of the PA (Di Gesu et al. 2023). Given such interesting variability patterns, it is important to continue to follow the X-ray and multiwavelength polarization, as well as the SED, of Mrk 501 via long-term monitoring, in order to determine whether the consistency of the magnetic field geometry and its relation to particle acceleration remains stable or varies over a longer timescale than sampled thus far. It is also important to continue to develop theories and simulations to explore further the properties of the shock-plus-turbulence model and perhaps to find other physical scenarios that can reproduce the multiwavelength polarization properties reported here.

Acknowledgments

The Imaging X-ray Polarimetry Explorer (IXPE) is a joint US and Italian mission. The US contribution is supported by the National Aeronautics and Space Administration (NASA) and led and managed by its Marshall Space Flight Center (MSFC), with industry partner Ball Aerospace (contract NNM15AA18C). The Italian contribution is supported by the Italian Space Agency (Agenzia Spaziale Italiana, ASI) through contract ASI-OHBI-2017-12-I.0, agreements ASI-INAF-2017-12-H0 and ASI-INFN-2017.13-H0, its Space Science Data Center (SSDC), and by the Istituto Nazionale di Astrofisica (INAF) and the Istituto Nazionale di Fisica Nucleare (INFN) in Italy.

This research used data products provided by the IXPE Team (MSFC, SSDC, INAF, and INFN) and distributed with additional software tools by the High-Energy Astrophysics Science Archive Research Center (HEASARC), at NASA Goddard Space Flight Center (GSFC). The IAA-CSIC group acknowledges financial support from the grant CEX2021-001131-S funded by MCIN/AEI/10.13039/501100011033 to the Instituto de Astrofísica de Andalucía-CSIC and through grant PID2019-107847RB-C44. The POLAMI observations were carried out at the IRAM 30 m Telescope. IRAM is supported by INSU/CNRS (France), MPG (Germany), and IGN (Spain). The Submillimeter Array is a joint project between the Smithsonian Astrophysical Observatory and the Academia Sinica Institute of Astronomy and Astrophysics and is funded by the Smithsonian Institution and the Academia Sinica. Maunakea, the location of the SMA, is a culturally important site for the indigenous Hawaiian people; we are privileged to study the cosmos from its summit. Some of the data reported here are based on observations made with the Nordic Optical Telescope, owned in collaboration with the University of Turku and Aarhus University, and operated jointly by Aarhus University, the University of Turku, and the University of Oslo, representing Denmark, Finland, and Norway, the University of Iceland and Stockholm University at the Observatorio del Roque de los Muchachos, La Palma, Spain, of the Instituto de Astrofisica de Canarias. E.L. was supported by Academy of Finland projects 317636 and

320045. The data presented here were obtained in part with ALFOSC, which is provided by the Instituto de Astrofisica de Andalucia (IAA) under a joint agreement with the University of Copenhagen and NOT. Part of the French contribution is supported by the Scientific Research National Center (CNRS) and the French spatial agency (CNES). The USRA coauthors gratefully acknowledge NASA funding through contract 80NSSC24M0035. The research at Boston University was supported in part by National Science Foundation grant AST-2108622, NASA Fermi Guest Investigator grants 80NSSC23K1507 and 80NSSC22K1571, and NASA Swift Guest Investigator grant 80NSSC22K0537. This study was based in part on observations conducted using the 1.8 m Perkins Telescope Observatory (PTO) in Arizona, which is owned and operated by Boston University. This work was supported by JST, the establishment of university fellowships toward the creation of science and technology innovation, grant No. JPMJFS2129. This work was supported by Japan Society for the Promotion of Science (JSPS) KAKENHI grant Nos. JP21H01137. This work was also partially supported by the Optical and Near-Infrared Astronomy Inter-University Cooperation Program from the Ministry of Education, Culture, Sports, Science and Technology (MEXT) of Japan. We are grateful to the observation and operating members of the Kanata Telescope. Some of the data are based on observations collected at the Observatorio de Sierra Nevada, owned and operated by the Instituto de Astrofísica de Andalucía (IAA-CSIC). Further data are based on observations collected at the Centro Astronómico Hispano en Andalucía (CAHA), operated jointly by Junta de Andalucía and Consejo Superior de Investigaciones Científicas (IAA-CSIC). C.C. acknowledges support from the European Research Council (ERC) under the HORIZON ERC grants 2021 program under grant agreement No. 101040021. This work was supported by NSF grant AST-2109127. We acknowledge the use of public data from the Swift data archive. Based on observations obtained with XMM-Newton, an ESA science mission with instruments and contributions directly funded by ESA Member States and NASA. Data from the Steward Observatory spectropolarimetric monitoring project were used. This program was supported by Fermi Guest Investigator grants NNX08AW56G, NNX09AU10G, NNX12AO93G, and NNX15AU81G. We acknowledge the funding to support our NOT observations from the Academy of Finland grant 306531. The Very Long Baseline Array is an instrument of the National Radio Astronomy Observatory. The National Radio Astronomy Observatory is a facility of the National Science Foundation operated under a cooperative agreement by Associated Universities, Inc. S. K., S.-S. L., W. Y. C., S.-H. K., and H.-W. J. were supported by the National Research Foundation of Korea (NRF) grant funded by the Korea government (MIST) (2020R1A2C2009003). The KVN is a facility operated by the Korea Astronomy and Space Science Institute. The KVN operations are supported by KREONET (Korea Research Environment Open NETwork), which is managed and operated by KISTI (Korea Institute of Science and Technology Information). Partly based on observations with the 100 m telescope of the MPIfR (Max-Planck-Institut für Radioastronomie) at Effelsberg. Observations with the 100 m radio telescope at Effelsberg have received funding from the European Union's Horizon 2020 research and innovation program under grant agreement No 101004719 (ORP). The Dipol-2 polarimeter was built in cooperation by the University of Turku, Finland, and the Leibniz Institut für Sonnenphysik, Germany, with support from the Leibniz Association grant SAW-2011-KIS-7. I.L. was supported by the NASA Postdoctoral Program at the Marshall Space Flight Center, administered by Oak Ridge Associated Universities under contract with NASA.

Facilities: CAO:2.2m, Effelsberg, IRAM:30m, IXPE, KANATA, KVN, LX-200, NOT, NuSTAR, Perkins, SMA, OSN:0.9m, Swift (XRT and UVOT), TU:0.6m, XMM

Software: astropy (Astropy Collaboration et al. 2013; Astropy Collaboration 2018), ixpeobssim, xspec.

Appendix
Supplementary Figures for X-Ray and Multiwavelength Data

We show the complete multiwavelength data in the radio and optical–IR bands in Figure A1. Spectropolarimetric data and best-fit models for individual IXPE observations and their ancillary data are also shown in Figures A2 and A3.

As shown in Figure A1, some IXPE observations were covered with multiple optical measurements. Specifically, there are 14, 1, 4, 7, 2, and 5 *R*-band observations from IXPE1 to IXPE6, respectively. We did not see substantial variations in the optical PD and PA. During IXPE4, PD_{opt} appears to have increased. However, within the IXPE4 measurement, the observation with the most significant deviation from the average value also exhibited large uncertainties, placing it only 1.6σ away from the average. For the radio data, no single IXPE observation included more than one radio measurement at the same frequency. IXPE4 and IXPE5 do have additional radio measurements immediately before or after the IXPE observations. However, they are within 1σ uncertainty of the radio measurements contemporaneous to the IXPE observations. The lack of apparent correlations between different wavelengths is still consistent with the energy-stratified shock scenario, in which emission at different wavelengths is thought to originate from different regions.

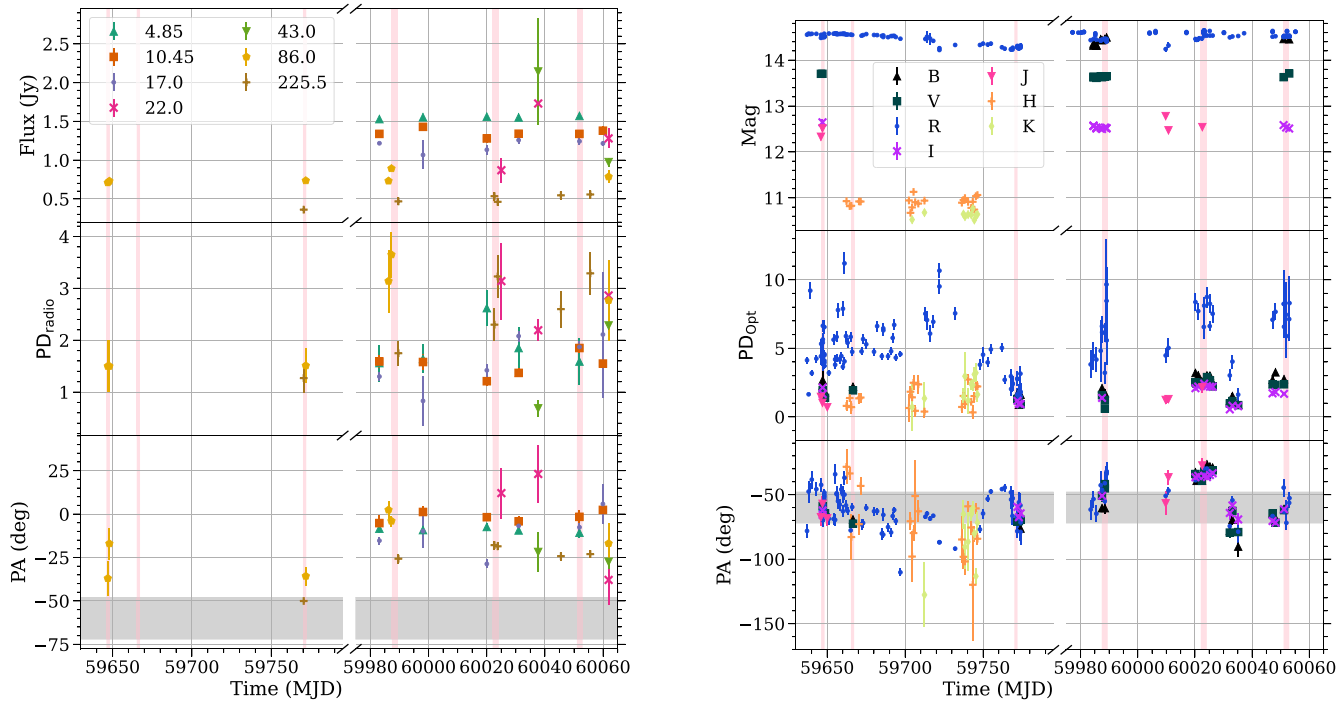

Figure A1. Multiwavelength photometric and polarimetric measurements as a function of time. The pink regions mark the durations of the three IXPE observations. The error bars indicate the 68% confidence (1σ) uncertainty. The jet axis is marked as the gray region in the bottom panels. Left: radio observations of Mrk 501 in 2023; observations at different frequencies (in gigahertz) are marked with different symbols shown in the figure legend. The top panel shows the flux density in Janskys, the middle panel the degree of polarization, and the bottom panel the PA. The error bars indicate the 68% confidence (1σ) uncertainty. Right: optical and IR observations of Mrk 501 in 2023. The top panel shows the brightness in magnitudes, the middle panel the degree of polarization (in percent), and the bottom panel the PA.

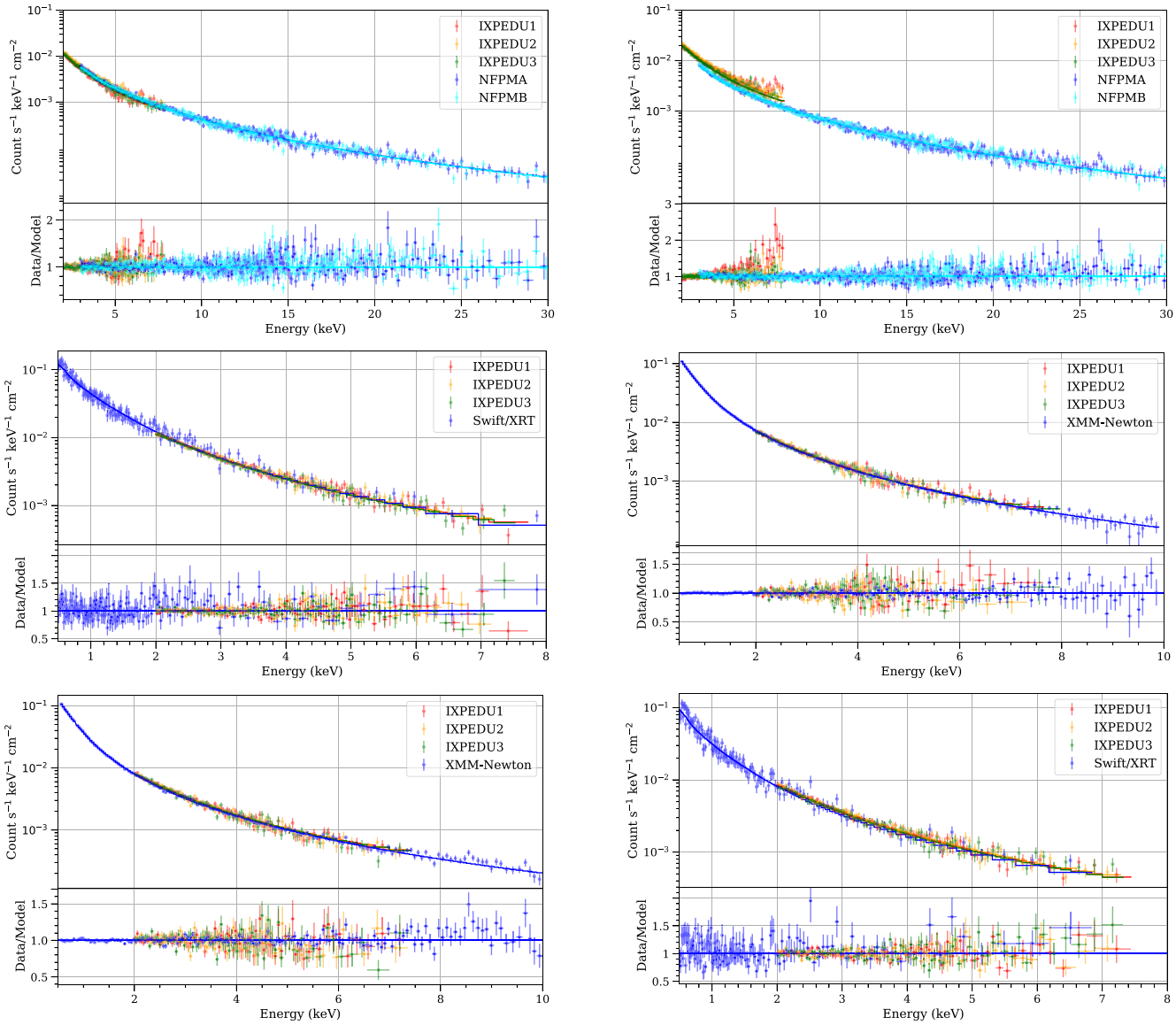

Figure A2. X-ray spectra and best-fit model for each IXPE Mrk 501 observation. Shown here are the IXPE Stokes *I* spectra and ancillary X-ray data. Different instruments are color-coded, with the data and model ratio shown in the bottom panel for each plot. See Section 3.1 for details.

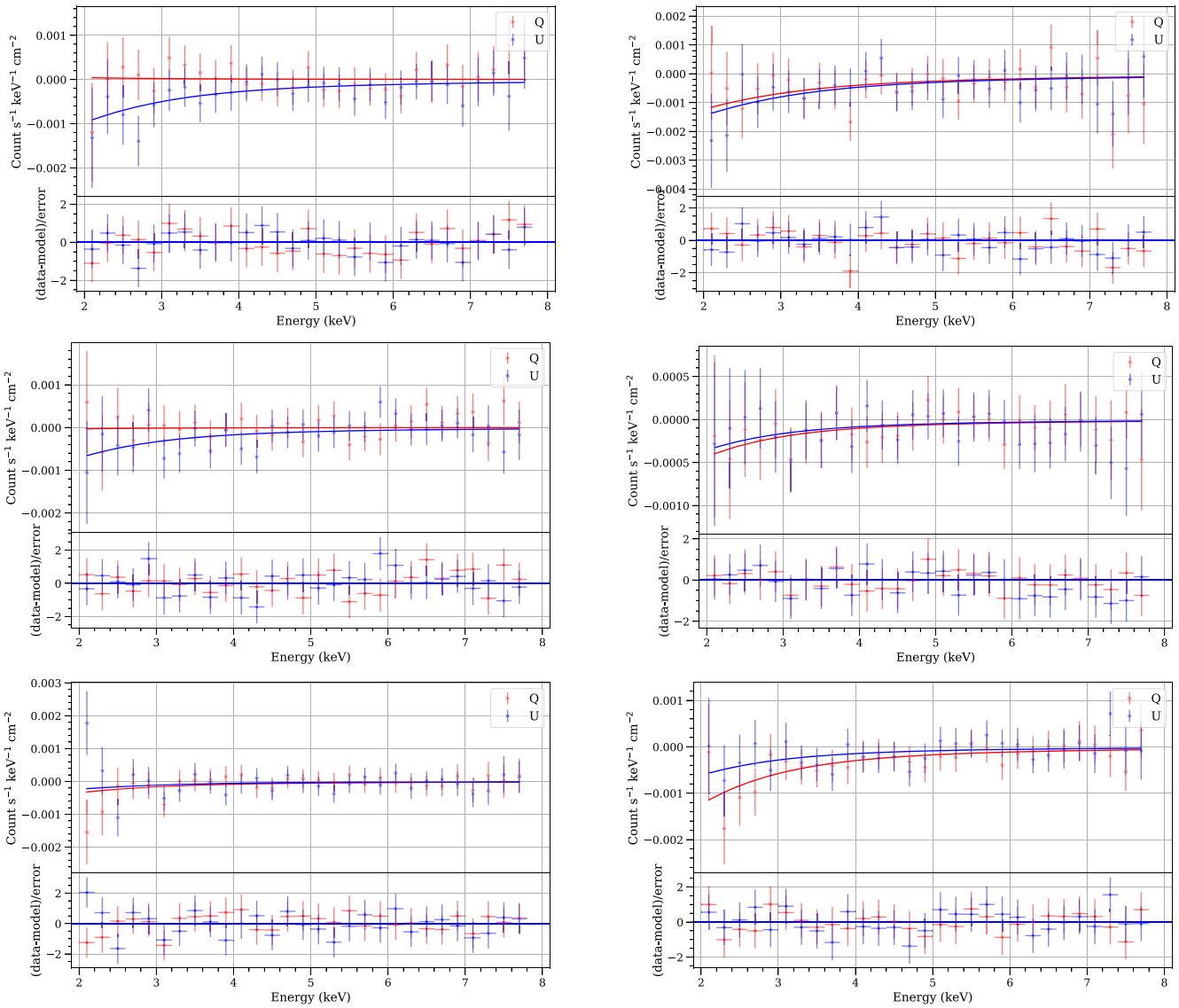

Figure A3. Similar to Figure A2, but only showing the IXPE Stokes Q and U spectra.

ORCID iDs

Chien-Ting J. Chen https://orcid.org/0000-0002-4945-5079
Ioannis Liodakis https://orcid.org/0000-0001-9200-4006
Riccardo Middei https://orcid.org/0000-0001-9815-9092
Dawoon E. Kim https://orcid.org/0000-0001-5717-3736
Laura Di Gesu https://orcid.org/0000-0002-5614-5028
Alessandro Di Marco https://orcid.org/0000-0003-0331-3259
Steven R. Ehlert https://orcid.org/0000-0003-4420-2838
Manel Errando https://orcid.org/0000-0002-1853-863X
Michela Negro https://orcid.org/0000-0002-6548-5622
Svetlana G. Jorstad https://orcid.org/0000-0001-6158-1708
Alan P. Marscher https://orcid.org/0000-0001-7396-3332
Kinwah Wu https://orcid.org/0000-0002-7568-8765
Iván Agudo https://orcid.org/0000-0002-3777-6182
Juri Poutanen https://orcid.org/0000-0002-0983-0049
Tsunefumi Mizuno https://orcid.org/0000-0001-7263-0296
Pouya M. Kouch https://orcid.org/0000-0002-9328-2750
George A. Borman https://orcid.org/0000-0002-7262-6710
Tatiana S. Grishina https://orcid.org/0000-0002-3953-6676
Evgenia N. Kopatskaya https://orcid.org/0000-0001-9518-337X
Elena G. Larionova https://orcid.org/0000-0002-2471-6500
Daria A. Morozova https://orcid.org/0000-0002-9407-7804
Sergey S. Savchenko https://orcid.org/0000-0003-4147-3851
Ivan S. Troitsky https://orcid.org/0000-0002-4218-0148
Yulia V. Troitskaya https://orcid.org/0000-0002-9907-9876
Andrey A. Vasilyev https://orcid.org/0000-0002-8293-0214
Giacomo Bonnoli https://orcid.org/0000-0003-2464-9077
Juan Escudero https://orcid.org/0000-0002-4131-655X
Beatriz Agís-González https://orcid.org/0000-0001-7702-8931
César Husillos https://orcid.org/0000-0001-8286-5443
Vilppu Piirola https://orcid.org/0000-0003-0186-206X
Ioannis Myserlis https://orcid.org/0000-0003-3025-9497
Alexander Kraus https://orcid.org/0000-0002-4184-9372
Mark Gurwell https://orcid.org/0000-0003-0685-3621
Garrett Keating https://orcid.org/0000-0002-3490-146X
Sincheol Kang https://orcid.org/0000-0002-0112-4836
Sang-Sung Lee https://orcid.org/0000-0002-6269-594X
Sang-Hyun Kim https://orcid.org/0000-0001-7556-8504
Whee Yeon Cheong https://orcid.org/0009-0002-1871-5824
Hyeon-Woo Jeong https://orcid.org/0009-0005-7629-8450
Chanwoo Song https://orcid.org/0009-0003-8767-7080

Andrei V. Berdyugin https://orcid.org/0000-0002-9353-5164
Vadim Kravtsov https://orcid.org/0000-0002-7502-3173
Anagha P. Nitindala https://orcid.org/0009-0002-7109-0202
Ryo Imazawa https://orcid.org/0000-0002-0643-7946
Yasushi Fukazawa https://orcid.org/0000-0002-0921-8837
Koji S. Kawabata https://orcid.org/0000-0001-6099-9539
Makoto Uemura https://orcid.org/0000-0002-7375-7405
Hiroshi Akitaya https://orcid.org/0000-0001-6156-238X
Carolina Casadio https://orcid.org/0000-0003-1117-2863
Lucio Angelo Antonelli https://orcid.org/0000-0002-5037-9034
Matteo Bachetti https://orcid.org/0000-0002-4576-9337
Luca Baldini https://orcid.org/0000-0002-9785-7726
Wayne H. Baumgartner https://orcid.org/0000-0002-5106-0463
Ronaldo Bellazzini https://orcid.org/0000-0002-2469-7063
Stefano Bianchi https://orcid.org/0000-0002-4622-4240
Stephen D. Bongiorno https://orcid.org/0000-0002-0901-2097
Raffaella Bonino https://orcid.org/0000-0002-4264-1215
Alessandro Brez https://orcid.org/0000-0002-9460-1821
Niccoló Bucciantini https://orcid.org/0000-0002-8848-1392
Fiamma Capitanio https://orcid.org/0000-0002-6384-3027
Simone Castellano https://orcid.org/0000-0003-1111-4292
Elisabetta Cavazzuti https://orcid.org/0000-0001-7150-9638
Stefano Ciprini https://orcid.org/0000-0002-0712-2479
Enrico Costa https://orcid.org/0000-0003-4925-8523
Alessandra De Rosa https://orcid.org/0000-0001-5668-6863
Ettore Del Monte https://orcid.org/0000-0002-3013-6334
Niccoló Di Lalla https://orcid.org/0000-0002-7574-1298
Immacolata Donnarumma https://orcid.org/0000-0002-4700-4549
Victor Doroshenko https://orcid.org/0000-0001-8162-1105
Michal Dovčiak https://orcid.org/0000-0003-0079-1239
Teruaki Enoto https://orcid.org/0000-0003-1244-3100
Yuri Evangelista https://orcid.org/0000-0001-6096-6710
Sergio Fabiani https://orcid.org/0000-0003-1533-0283
Riccardo Ferrazzoli https://orcid.org/0000-0003-1074-8605
Javier A. Garcia https://orcid.org/0000-0003-3828-2448
Shuichi Gunji https://orcid.org/0000-0002-5881-2445
Jeremy Heyl https://orcid.org/0000-0001-9739-367X
Wataru Iwakiri https://orcid.org/0000-0002-0207-9010
Philip Kaaret https://orcid.org/0000-0002-3638-0637
Vladimir Karas https://orcid.org/0000-0002-5760-0459
Fabian Kislat https://orcid.org/0000-0001-7477-0380
Jeffery J. Kolodziejczak https://orcid.org/0000-0002-0110-6136
Henric Krawczynski https://orcid.org/0000-0002-1084-6507
Fabio La Monaca https://orcid.org/0000-0001-8916-4156
Luca Latronico https://orcid.org/0000-0002-0984-1856
Simone Maldera https://orcid.org/0000-0002-0698-4421
Alberto Manfreda https://orcid.org/0000-0002-0998-4953
Frédéric Marin https://orcid.org/0000-0003-4952-0835
Andrea Marinucci https://orcid.org/0000-0002-2055-4946
Herman L. Marshall https://orcid.org/0000-0002-6492-1293
Francesco Massaro https://orcid.org/0000-0002-1704-9850
Giorgio Matt https://orcid.org/0000-0002-2152-0916
Fabio Muleri https://orcid.org/0000-0003-3331-3794
C.-Y. Ng https://orcid.org/0000-0002-5847-2612
Stephen L. O'Dell https://orcid.org/0000-0002-1868-8056
Nicola Omodei https://orcid.org/0000-0002-5448-7577
Chiara Oppedisano https://orcid.org/0000-0001-6194-4601
Alessandro Papitto https://orcid.org/0000-0001-6289-7413
George G. Pavlov https://orcid.org/0000-0002-7481-5259
Abel Lawrence Peirson https://orcid.org/0000-0001-6292-1911
Matteo Perri https://orcid.org/0000-0003-3613-4409
Melissa Pesce-Rollins https://orcid.org/0000-0003-1790-8018
Pierre-Olivier Petrucci https://orcid.org/0000-0001-6061-3480
Maura Pilia https://orcid.org/0000-0001-7397-8091
Andrea Possenti https://orcid.org/0000-0001-5902-3731
Simonetta Puccetti https://orcid.org/0000-0002-2734-7835
Brian D. Ramsey https://orcid.org/0000-0003-1548-1524
John Rankin https://orcid.org/0000-0002-9774-0560
Ajay Ratheesh https://orcid.org/0000-0003-0411-4243
Oliver J. Roberts https://orcid.org/0000-0002-7150-9061
Roger W. Romani https://orcid.org/0000-0001-6711-3286
Carmelo Sgró https://orcid.org/0000-0001-5676-6214
Patrick Slane https://orcid.org/0000-0002-6986-6756
Paolo Soffitta https://orcid.org/0000-0002-7781-4104
Gloria Spandre https://orcid.org/0000-0003-0802-3453
Douglas A. Swartz https://orcid.org/0000-0002-2954-4461
Toru Tamagawa https://orcid.org/0000-0002-8801-6263
Fabrizio Tavecchio https://orcid.org/0000-0003-0256-0995
Roberto Taverna https://orcid.org/0000-0002-1768-618X
Allyn F. Tennant https://orcid.org/0000-0002-9443-6774
Nicholas E. Thomas https://orcid.org/0000-0003-0411-4606
Francesco Tombesi https://orcid.org/0000-0002-6562-8654
Alessio Trois https://orcid.org/0000-0002-3180-6002
Sergey S. Tsygankov https://orcid.org/0000-0002-9679-0793
Roberto Turolla https://orcid.org/0000-0003-3977-8760
Jacco Vink https://orcid.org/0000-0002-4708-4219
Martin C. Weisskopf https://orcid.org/0000-0002-5270-4240
Fei Xie https://orcid.org/0000-0002-0105-5826
Silvia Zane https://orcid.org/0000-0001-5326-880X

References

Agudo, I., Thum, C., Ramakrishnan, V., et al. 2018a, MNRAS, 473, 1850
Agudo, I., Thum, C., Molina, S. N., et al. 2018b, MNRAS, 474, 1427
Ajello, M., Angioni, R., Axelsson, M., et al. 2020, ApJ, 892, 105
Akitaya, H., Moritani, Y., Ui, T., et al. 2014, Proc. SPIE, 9147, 91474O
Astropy Collaboration, Price-Whelan, A. M., Sipőcz, B. M., et al. 2018, AJ, 156, 123
Astropy Collaboration, Robitaille, T. P., Tollerud, E. J., et al. 2013, A&A, 558, A33
Blandford, R., Meier, D., & Readhead, A. 2019, ARA&A, 57, 467
Burn, B. J. 1966, MNRAS, 133, 67
Di Gesu, L., Donnarumma, I., Tavecchio, F., et al. 2022b, ApJL, 938, L7
Di Gesu, L., Marshall, H. L., Ehlert, S. R., et al. 2023, NatAs, 7, 1245
Di Gesu, L., Tavecchio, F., Donnarumma, I., et al. 2022a, A&A, 662, A83
Di Marco, A., Soffitta, P., Costa, E., et al. 2023, AJ, 165, 143
Ehlert, S. R., Liodakis, I., Middei, R., et al. 2023, ApJ, 959, 61
Errando, M., Liodakis, I., Marscher, A. P., et al. 2024, ApJ, 963, 5
Ho, P. T. P., Moran, J. M., & Lo, K. Y. 2004, ApJL, 616, L1
Hovatta, T., & Lindfors, E. 2019, NewAR, 87, 101541
Hovatta, T., Lindfors, E., Blinov, D., et al. 2016, A&A, 596, A78
Kang, S., Lee, S.-S., & Byun, D.-Y. 2015, JKAS, 48, 257
Kawabata, K. S., Okazaki, A., Akitaya, H., et al. 1999, PASP, 111, 898
Kim, D. E., Di Gesu, L., Liodakis, I., et al. 2024, A&A, 681, A12
Kislat, F., Clark, B., Beilicke, M., & Krawczynski, H. 2015, APh, 68, 45
Kouch, P. M., Liodakis, I., Middei, R., et al. 2024, A&A, 689, A119
Kraus, A., Krichbaum, T. P., Wegner, R., et al. 2003, A&A, 401, 161
Liodakis, I., Marscher, A. P., Agudo, I., et al. 2022, Natur, 611, 677
Liodakis, I., Peirson, A. L., & Romani, R. W. 2019, ApJ, 880, 29
Lisalda, L., Gau, E., Krawczynski, H., et al. 2024, MNRAS, submitted
MAGIC Collaboration, Abe, S., Abhir, J., et al. 2024, A&A, 685, A117
Marscher, A. P. 2014, ApJ, 780, 87
Massaro, E., Perri, M., Giommi, P., Nesci, R., & Verrecchia, F. 2004, A&A, 422, 103
Middei, R., Marinucci, A., Braito, V., et al. 2022, MNRAS, 514, 2974
Middei, R., Perri, M., Puccetti, S., et al. 2023, ApJL, 953, L28

Myserlis, I., Angelakis, E., Kraus, A., et al. 2018, A&A, 609, A68
NASA High Energy Astrophysics Science Archive Research Center (HEASARC) 2014, HEAsoft: Unified Release of FTOOLS and XANADU, Astrophysics Source Code Library, ascl:1408.004
Nilsson, K., Lindfors, E., Takalo, L. O., et al. 2018, A&A, 620, A185
Nilsson, K., Pasanen, M., Takalo, L. O., et al. 2007, A&A, 475, 199
Peacock, J. A. 1983, MNRAS, 202, 615
Peirson, A. L., Liodakis, I., & Romani, R. W. 2022, ApJ, 931, 59
Peirson, A. L., & Romani, R. W. 2019, ApJ, 885, 76
Piirola, V., Berdyugin, A., & Berdyugina, S. 2014, Proc. SPIE, 9147, 91478I
Piirola, V., Berdyugin, A., Frisch, P. C., et al. 2020, A&A, 635, A46
Rybicki, G. B., & Lightman, A. P. 1979, Radiative processes in astrophysics (New York: Wiley)
Stroh, M. C., & Falcone, A. D. 2013, ApJS, 207, 28
Thum, C., Agudo, I., Molina, S. N., et al. 2018, MNRAS, 473, 2506
Tramacere, A., Giommi, P., Perri, M., Verrecchia, F., & Tosti, G. 2009, A&A, 501, 879
Weaver, Z. R., Jorstad, S. G., Marscher, A. P., et al. 2022, ApJS, 260, 12
Weisskopf, M. C., Soffitta, P., Baldini, L., et al. 2022, JATIS, 8, 026002
Zhang, H., & Böttcher, M. 2013, ApJ, 774, 18
Zhang, H., Fang, K., Li, H., et al. 2019, ApJ, 876, 109
Zhang, Y. H., Treves, A., Celotti, A., Qin, Y. P., & Bai, J. M. 2005, ApJ, 629, 686